Reaction sintering of rhabdophane into monazite-cheralite Nd1-2xThxCaxPO4 (x = 0 – 0.1) ceramics

Danwen Qin, Adel Mesbah, Joseph Lautru, Stephanie Szenknect, Nicolas Dacheux, Nicolas Clavier

Journal Pre-proof

Reaction sintering of rhabdophane into monazite-cheralite $Nd_{1-2x}Th_xCa_xPO_4$ (x = 0 – 0.1) ceramics

Danwen Qin, Adel Mesbah, Joseph Lautru, Stéphanie Szenknect, Nicolas Dacheux, Nicolas Clavier

PII: S0955-2219(19)30721-6

DOI: https://doi.org/10.1016/j.jeurceramsoc.2019.10.050

Reference: JECS 12812

To appear in: *Journal of the European Ceramic Society*

Received Date: 24 September 2019

Revised Date: 23 October 2019

Accepted Date: 25 October 2019

Please cite this article as: Qin D, Mesbah A, Lautru J, Szenknect S, Dacheux N, Clavier N, Reaction sintering of rhabdophane into monazite-cheralite $Nd_{1-2x}Th_xCa_xPO_4$ (x = 0 – 0.1) ceramics, *Journal of the European Ceramic Society* (2019), doi: https://doi.org/10.1016/j.jeurceramsoc.2019.10.050

Reaction sintering of rhabdophane into monazite-cheralite $Nd_{1-2x}Th_xCa_xPO_4$ (x = 0 – 0.1) ceramics

Danwen Qin, Adel Mesbah, Joseph Lautru, Stéphanie Szenknect,Nicolas Dacheux, Nicolas Clavier*

ICSM, CNRS, CEA, ENSCM, Univ Montpellier, Site de Marcoule, BP 17171, 30207 Bagnols sur Cèze, France

*** Corresponding author:**

Dr. Nicolas CLAVIER
ICSM, CEA, CNRS, ENSCM, Univ Montpellier
Site de Marcoule
BP 17171
30207 Bagnols sur Cèze
France

Phone : + 33 4 66 33 92 08
Fax : + 33 4 66 79 76 11

nicolas.clavier@icsm.fr

Abstract:

The direct sintering of $Nd_{1-2x}Ca_xTh_xPO_4 \cdot nH_2O$ rhabdophanes (x = 0 – 0.1) was achieved for the first time resulting in homogeneous high-density monazite-cheralite pellets. Thanks to their large specific surface area, rhabdophane precursors led to a lower shrinkage temperature compared to samples synthesized through solid-state reactions. The associated activation energy was found between 361 ± 90 and 530 ± 90 $kJ.mol^{-1}$, depending on the thorium incorporation. Meanwhile, sintering map was built up, showing that densification predominated for T ≤ 1200 °C. Conversely, the complete densification took place at 1400 °C concomitantly to grain growth and elimination of open porosity. Moreover, Th-Ca coupled substitution seemed to inhibit both densification and grain growth as the average grain size dropped down one order by one order of magnitude between x = 0.0 and x = 0.1. However, these

differences did not affect microhardness, which reached 4.9 ± 0.8 GPa whatever the chemical composition tested.

Keywords : thorium, phosphates, wasteform, sintering map, microstructure

1. Introduction

Monazite has been reported as a promising ceramic matrix for long-term radioactive waste management, especially for the specific conditioning of actinides [1]. Considered as the second most abundant mineral source of rare earth elements and the first one for thorium [2, 3], monazite fulfills several requirements as a radwaste matrix, *i.e.* a significant weight loading in actinides (AnO_2 > 16 wt. %, with An = Th/U in natural samples) [4, 5], high chemical durability [6, 7], and strong resistance to radiation damages [8].

The oxidation state of the actinide elements is a key factor during their incorporation into the monazite structure. If direct incorporation has been widely reported for trivalent actinide (*e.g.* Pu, Am) by forming $Ln_{1-x}An^{III}_{x}PO_4$ solid solutions [9, 10], that of tetravalent actinides is limited to several wt. %. A coupled substitution is then required to achieve the insertion of important amounts of An(IV) [11]. One of the two most documented mechanisms is to replace partially the lanthanide elements by divalent cation (e.g. alkaline earth metal) and tetravalent actinide to form $Ln_{1-2x}An^{IV}_{x}M^{II}_{x}PO_4$ monazite-cheralite solid solutions. The second one lies on the substitution of phosphate groups with silicate entities, leading to $Ln_{1-x}An^{IV}_{x}(PO_4)_{1-x}(SiO_4)_x$ monazite-huttonite solid solutions [4, 12, 13]. In our previous study, the first type of substitution was explored through hydrothermal syntheses, leading to single-phase Th-bearing rhabdophanes $Ln_{1-2x}Th_xCa_xPO_4{\cdot}nH_2O$ (Ln = Pr/Nd, x = 0 – 0.15) [14]. Later, the as-synthesized rhabdophanes were successfully converted into single-phase monazite-cheralite solid solutions, $Ln_{1-2x}Th_xCa_xPO_4$. Both dehydration and conversion steps of the rhabdophane precursors were monitored and investigated [15], showing that pure monazite-cheralite could be obtained by simply heating Th-rhabdophane synthesized in hydrothermal conditions at T = 1100°C. Nevertheless, the possibility to obtain high-density monazite-cheralite ceramics directly from the associated rhabdophane precursor remained unexplored.

Although, several studies have been dedicated to the sintering of monazite or monazite-cheralite ceramics. Hikichi *et al.* reported on the thermal, mechanical and chemical properties of sintered monazite end-members ($LnPO_4$ with Ln = La, Ce, Nd, and Sm) and pointed out the importance of the initial specific surface area of the precursor to obtain high-density ceramics. A monazite-type $NdPO_4$ precursor, converted from rhabdophane at 600°C for 2 h ($S_{SA} \approx 60\ m^2.g^{-1}$), led to a ceramic with a relative density close to 99 %TD (theoretical density) after sintering at 1200°C for 5h [16]. Bregiroux *et al.* investigated the effect of the synthesis route of precursors on the sintering ability of the monazite ceramic $LnPO_4$ (Ln = La, Ce, and Y) [17] and explored direct sintering from $LaPO_4{\cdot}nH_2O$ precursor. After heating at 1400°C for 1h, the ceramic obtained by direct sintering of the rhabdophane presented a relative density of 95.5 %TD while sintering from monazite required $Ln(PO_3)_3$ as a sintering aid or a pre-milling step to reach comparable density values. A similar conclusion was drawn by Arinicheva *et al.* who recently studied the sintering and mechanical properties of monazite-type $La_{1-x}Eu_xPO_4$. In their

study, the densification of the monazite powders was performed at 1350°C through hot pressing to reach dense ceramics (98 %TD) [18]. Later, Neumeier *et al.* modified this protocol to produce $La_{0.5}Eu_{0.5}PO_4$ pellets (with 92.5 %TD) by natural sintering at 1450°C for 5h [19]. The starting monazite powder was obtained from conversion of rhabdophane, leading to a large specific surface area of about 100 $m^2.g^{-1}$ [20].

Contrary to monazites, all reports concerning the sintering of monazite-cheralite ceramics involved dry chemistry routes based on solid-state reactions. For example, Montel *et al.* and Glorieux *et al.* reported the sintering of $La_{0.73}Ce_{0.09}Th_{0.09}Ca_{0.09}PO_4$ [21, 22], which first required long-time high-temperature heat treatments (1250 °C for one night) to obtain the precursor powder. Besides, several milling cycles were applied in order to ensure its homogeneity and to increase its specific surface area (6 – 7 $m^2.g^{-1}$). Sintering was finally undertaken at 1450°C for 4h to reach a final relative density above 95 %TD.

According to these results, direct sintering of rhabdophanes into $Nd_{1-2x}Th_xCa_xPO_4$ monazite-cheralite ceramics is then expected to provide several advantages such as a large initial specific surface area which favors powders sintering, no need for high-temperature heat treatment and milling cycles, as well as a good homogeneity of the final powder in terms of cations distribution. Besides, the scarce works related to Th-bearing monazite-cheralite ceramics were usually based on a unique composition. The effect of the coupled substitution on sintering then needed to be investigated. In this frame, sintering map, which represents the variation of the average grain size as a function of the relative density under various experimental conditions (e.g. chemical composition, temperature, time, etc.), appears as an useful tool to develop the understanding of Th-doping influence and monitor the final microstructure of the ceramics. Nevertheless, few studies have been done on radioactive materials. In our knowledge, only Clavier *et al.* have reported the sintering map of ThO_2 [23] while Cherkaski *et al.* published the diagram of $Th_{1-x}Y_xO_{2-x/2}$ [24]. Consequently, the sintering map of $Nd_{1-2x}Th_xCa_xPO_4$ (x = 0 - 0.1) solid solutions will be established in this study.

Finally, if several authors reported on the mechanical properties of $LnPO_4$ monazite end-members [13, 18, 25], no data is available for monazite-cheralite solid solutions. As such data remain of primary importance to anticipate the microstructural evolution of the ceramic wasteform under chemical or radiative stresses, and provide insights on its sustainability, the microhardness of $Nd_{1-2x}Th_xCa_xPO_4$ was also determined.

2. Experiments

2.1. Synthesis of rhabdophane-type $Nd_{1-2x}Th_xCa_xPO_4{\cdot}nH_2O$ precursors

The synthesis of $Nd_{1-2x}Th_xCa_xPO_4{\cdot}nH_2O$ rhabdophane precursors followed the procedure reported in our previous works [14]. All the metal salts were provided by Sigma-Aldrich and were of analytical grade, *i.e.* $NdCl_3{\cdot}6\ H_2O$, $CaCl_2{\cdot}2\ H_2O$, $Th(NO_3)_4{\cdot}4\text{-}5\ H_2O$ while acid solutions were prepared from H_3PO_4 (85% Sigma-Aldrich), HCl (37% Carlo-Erba), and HNO_3 (69.5% Carlo-Erba). With the aim of avoiding their hygroscopic behavior, especially for thorium nitrate and neodymium chloride, the metal salts were dissolved in acid solutions (*i.e.* $NdCl_3$ and $CaCl_2$ in 0.1 M HCl, $Th(NO_3)_4$ in 4 M HNO_3). The concentrations of these solutions were further determined by ICP-OES measurements.

During the hydrothermal synthesis, thorium, and neodymium acidic solutions were first introduced into a Teflon® jar in the desired stoichiometric ratio. The calcium solution was then added with a 1000 % excess regarding to thorium amount. Indeed, from our previous works, the initial Ca:Th ratio was found to be a prevailing factor driving the calcium incorporation in the rhabdophane-type precursor, probably through the modification of Ca speciation in solution. Such a large excess was then adopted to fully operate the charge compensation, but also to promote the crystallization of the solid [14]. Finally, 5M H_3PO_4 with a 3% molar excess regarding Nd^{3+} and Th^{4+} was added dropwise. The mixture was stirred for 15 minutes then sealed in the hydrothermal reactor and heated in an oven at 110°C for 4 days. The obtained rhabdophane precipitates were washed twice with distilled water and once with ethanol, then dried at 90°C overnight. Finally, the obtained powder was ground manually in an agate mortar.

2.2. X-ray diffraction

XRD analyses were performed on powders and pellets using a Bruker D8 ADVANCE diffractometer with Cu Kα radiation (λ = 1.54184 Å). Powders were placed in a dedicated sample holder to avoid any radioactive contamination. This dome-shaped container equipped with an anti-scattering blade still can led to enhanced background as well as small variations in peaks intensities. On the other hand, pellet samples were previously polished to reach a mirror-grade surface and analyzed without the anti-contamination device. The same reflection geometry was applied for these two kinds of samples with 2θ ranging from 5 to 100° for data collection. A Δθ step of 0.019° with a collection time of 3.68 s per step was considered. In addition, a powder pattern of pure silicon was collected in similar conditions and used as an external standard to extract the instrumental function. The collected patterns were refined by the Rietveld method using the Fullprof_Suite package [26].

2.3. Pellets preparation

Before the heat treatments, rhabdophane precursors were pelletized by uniaxial pressing (500 MPa) at room temperature. For dilatometric studies, a typical mass of about 200 mg was used into Ø5 mm die, resulting in green pellets of about 2 mm in thickness (green density ≈ 60-65 %TD). For the establishment of sintering maps, Ø8 mm die was used in order to produce larger pellets and facilitate further manual polishing step. In this case, about 300 mg of powder was used while applied pressure remained unchanged, resulting in similar green densities.

2.4. Density measurements

Mass of sintered pellets was first measured by Mettler Toledo analytical balance. The bulk volume was then determined by geometric measurements with the help of a precision caliper, leading to bulk density values. In parallel, the helium density, which eliminates the contribution of the open pore volume, was determined by helium pycnometry, thanks to a Micromeritics Accupyc 1340 apparatus. The theoretical density (TD) was calculated by using the unit cell volumes as follows:

$$d_{th.} = \frac{M \times Z}{N_A \times V} \quad (1)$$

where M is the molar mass of the compound, Z the number of formula units per cell, N_A the Avogadro number and V the unit cell volume. These volumes were either selected from previous publications or calculated by linear interpolation between $NdPO_4$ and $Ca_{0.5}Th_{0.5}PO_4$ end members [27, 28]. Finally, bulk and helium densities were used to deduce the respective contributions of open and closed porosities.

2.5. Dilatometry

Dilatometric measurements were conducted on a Setaram Setsys Evolution apparatus with the aim to determine the temperature range to be used for the establishment of $Nd_{1-2x}Ca_xTh_xPO_4$ sintering maps. Green pellets were initially disposed between two alumina platelets and then heated up to 1400 °C under airflow, with a heating rate of 5 °C min^{-1}. The same rate was applied to cooling in order to avoid thermal fracture.

The activation energy associated with the densification was also determined thanks to the Dorn's method, which is based on several incremental isothermal heat treatments (1000-1500°C). According to the Johnson's model, the linear shrinkage under isothermal process is a function of time:

$$\frac{\Delta l}{l_0} = k(T)t^n \quad (2)$$

Therefore, the velocity of densification could be expressed by:

$$v = \frac{d\left(\frac{\Delta l}{l_0}\right)}{dt} = nk(T)\left(\frac{\Delta l}{l_0}\right)^{\frac{n-1}{n}} \quad (3)$$

Supposing that the grain growth during densification is negligible, so that:

$$k(T) = \frac{k_0}{T}\exp\left(-\frac{E_A}{RT}\right) \quad (4)$$

In this study, the temperature gap between the two successive isothermal treatments T_1 and T_2 is small enough (50°C) and the heating rate is high (30°C/min) which leads to:

$$\left(\frac{\Delta l}{l_0}\right)_{end\ step\ T_1} = \left(\frac{\Delta l}{l_0}\right)_{beginning\ step\ T_2} \quad (5)$$

The ratio between the associated velocities of densification could be presented as:

$$\frac{v_2}{v_1} = \frac{T_1}{T_2}\exp\left(-\frac{E_A}{R}\left(\frac{1}{T_2} - \frac{1}{T_1}\right)\right) \quad (6)$$

Consequently, the activation energy could be deduced:

$$E_A = \frac{RT_1T_2}{T_1 - T_2}\ln\left(\frac{v_1T_1}{v_2T_2}\right) \quad (7)$$

2.6. Electronic microscopy and image processing

Prior to SEM observations, sintered pellets were polished to reach an optical grade (with a 1 µm diamond spray). Grain boundaries were further revealed by thermal etching during 8h at 1000°C under air atmosphere which was considered not to modify significantly the microstructure of the samples. Several images (typically 4-8) were recorded on each sample in order to reach good representativeness. High vacuum conditions, associated with a very low accelerating voltage (2kV), were chosen to obtain high-resolution images.

SEM images were then processed using ImageJ software in order to assess the grain size distribution [29]. In this aim, grain boundaries were manually drawn in order to collect 300-1000 grains at the surface of each sample. The data collection depended on the image quality and the sintering conditions applied to the sample. The equivalent diameter of each grain (D) was calculated as follow, based the grain surface (A) measured by ImageJ:

$$D = 2\left(\frac{A}{\pi}\right)^{1/2} \quad (8)$$

The mass median diameter D_{50} was considered as the "average" diameter as it corresponds to 50 % of the cumulative frequency in a log-normal distribution. The mean grain size $\overline{D}$ was also determined as the mean value of the whole collected grain sizes.

2.7. Microhardness (H_V)

Microhardness was measured with a Vickers diamond indenter (Shimadzu HMV-G21D). The polished surface of the pellets was indented with a loading force of 0.1 – 2 N to determine the optimal value. The full indentation load was applied for 5 s. For each indenting force, ten measurements were performed in order to obtain the average value. Microhardness (H_V, expressed in GPa) was calculated using the following formula:

$$H_V = 18.544 \cdot \frac{F}{d_c^2} \quad (9)$$

Where F (N) is the applied load, d_c (µm) is the average length of Vickers indenter's diagonal.

3. Results and discussions

3.1. Characterization of powders and pellet samples

The rhabdophane powders and associated monazite-cheralite ceramic pellets (sintered at 1400°C for 8h) were first characterized by XRD. The XRD patterns (**Figure 1**) first confirmed that rhabdophane precursors crystallize in the monoclinic C2 structure as reported in our previous study [30]. Moreover, the pellets obtained after sintering were systematically found to be single-phase monazite-cheralite solid solutions (Monoclinic $P2_1/n$) [31], as no secondary phase, such as α-ThP_2O_7 [32], β-$Th_2(PO_4)(P_3O_{10})$ [33], β-$Th_4(PO_4)_4(P_2O_7)$ [34] or $Nd(PO_3)_3$ [35] was detected. As the conditions chosen constitute the most extreme used in this work in terms of temperature and heat duration, this result then ensures that single-phase samples will be obtained whatever the operating conditions. Also, the small differences noted in the peak intensities, especially for the x = 0.05 sample, were not considered to be significant, and were assigned to the use of an anti-contamination device during the measurements.

Meanwhile, the chemical composition of the rhabdophane samples was determined by total dissolution. For each component, about 20 mg of powder was dissolved in 2.5 mL of fresh aqua regia. These solutions were then diluted with 1% HNO_3 and analyzed by ICP-OES. The chemical compositions followed the expected stoichiometry considering the attached uncertainties (**Table 1**). Especially, the P/(Ca+Th+Nd) ratio was always found to be equal to 1, which excluded the formation of PO_3 metaphosphate entities that could hamper densification and grain growth processes [22].

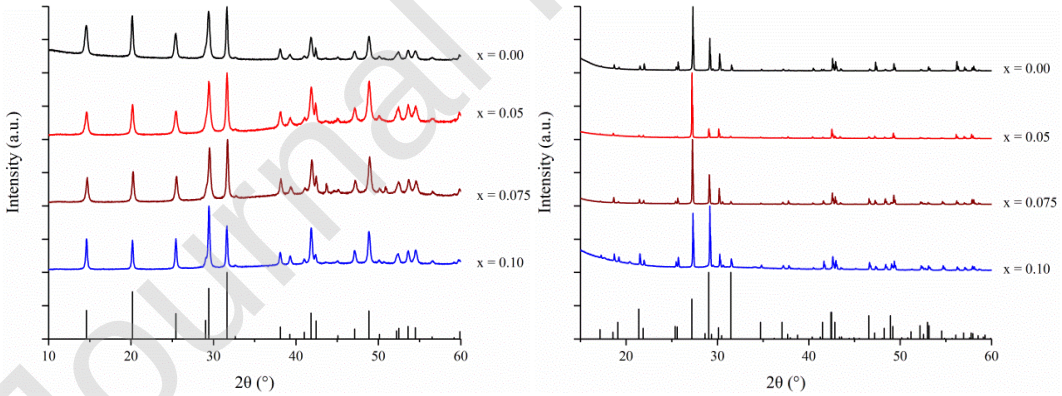

Figure 1. PXRD patterns obtained for $Nd_{1-2x}Th_xCa_xPO_4 \cdot nH_2O$ rhabdophane (left) [30] and associated $Nd_{1-2x}Th_xCa_xPO_4$ monazite-cheralite ceramic pellets obtained after conversion/sintering (right) [36].

Table 1. Chemical composition of the prepared $Nd_{1-2x}Th_xCa_xPO_4 \cdot nH_2O$ rhabdophane-type samples obtained by ICP-OES analysis after the full dissolution of the powdered samples.

x (target value)	Ca	Th	Nd	P/(Ca+Th+Nd)
0.05	0.07 ± 0.02	0.05 ± 0.01	0.88 ± 0.01	0.99 ± 0.01
0.075	0.10 ± 0.02	0.08 ± 0.01	0.82 ± 0.01	1.00 ± 0.01
0.10	0.10 ± 0.02	0.10 ± 0.01	0.80 ± 0.01	1.02 ± 0.01

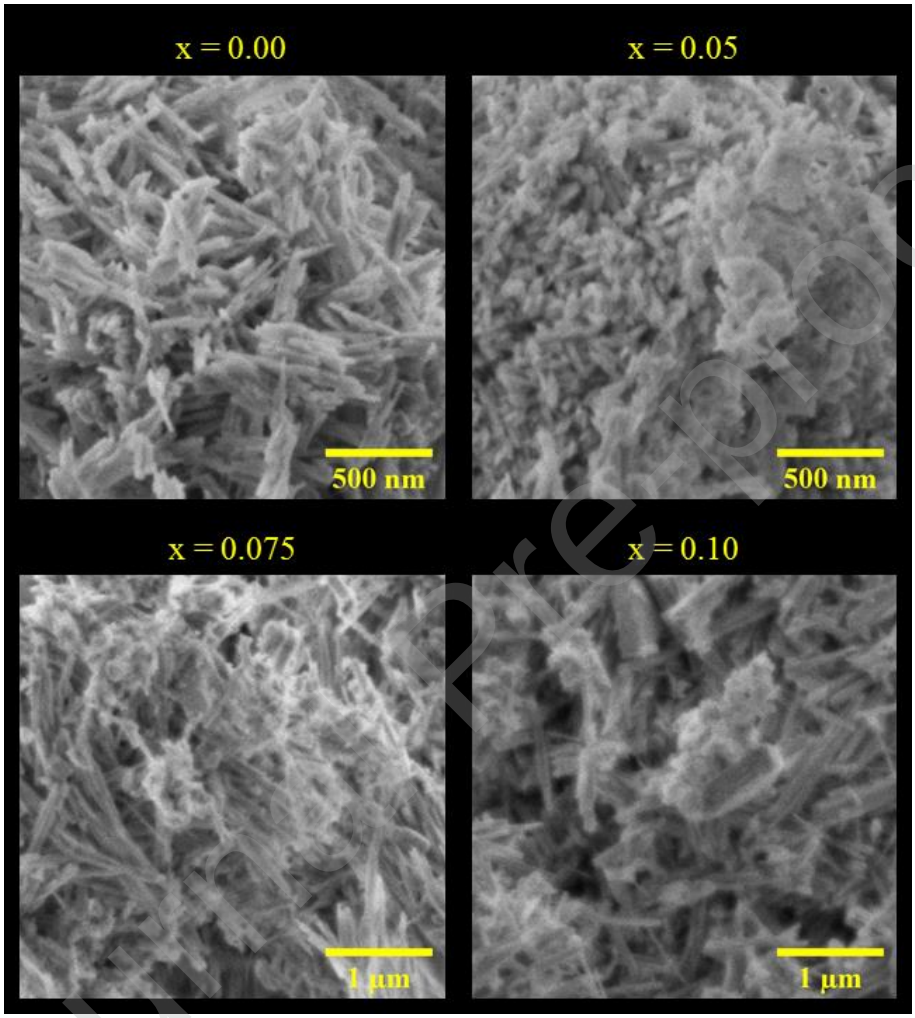

Figure 2. SEM micrographs of $Nd_{1-2x}Ca_xTh_xPO_4 \cdot nH_2O$ rhabdophane-type precursors.

Table 2. Specific surface area of $Nd_{1-2x}Th_xCa_xPO_4 \cdot nH_2O$ rhabdophane-type precursors.

x (target value)	0.00	0.05	0.075	0.10
Specific surface area ($m^2 \cdot g^{-1}$)	55 ± 1	51 ± 1	26 ± 1	24 ± 1

The SEM images (**Figure 2**) revealed that the as-synthesized precursors exhibited the typical needle-like morphology of rhabdophane samples (their generic name originating from the greek rhabdos which means stick/rod). The average length of the crystals reached about 500 nm for $NdPO_4$ and 100 nm for x = 0.05, while for x = 0.075 and x = 0.1, it was found about 1 µm. Hence, no clear correlation can be established between the Th/Ca incorporation and the crystal growth process during the hydrothermal synthesis. The associated specific surface area (S_{SA}) of the precursors was found between 24 and 55 $m^2.g^{-1}$, according to the BET measurements (**Table 2**), which should be in favor of efficient densification during sintering. Also, these values appeared clearly higher than those determined from samples synthesized through solid-state reaction which were usually reported below 20 m^2g^{-1} [17, 21, 22, 25].

3.2. Dilatometric study

A dilatometric study was further undertaken in order to determine the operating conditions leading to fully densified monazite-cheralite pellets directly from the as-synthesized rhabdophane powders. The variation of the relative linear shrinkage of the pellets versus temperature and the associated derivative is presented in **Figure 3**. All the samples followed a similar trend which contained three successive steps. The first one was assigned to the dehydration process leading from the monoclinic $Nd_{1-2x}Th_xCa_xPO_4 \cdot nH_2O$ to the hexagonal $Nd_{1-2x}Th_xCa_xPO_4$, which took place between 100 and 300°C [37]. In this range of temperatures, the vaporization of water is not expected to impact the pellets microstructure, neither by modifying the porosity network or by creating microscopic defects such as cracks. Indeed, as the green density approached 60% of the theoretical value, the water can be easily evacuated through the large amount of open pores still present in the solid. Also, this dehydration step was only associated with a small swelling of the pellet which is accommodated without any significant modification of the morphology.

The second step was associated to a 2.5 – 7.5 % relative linear shrinkage, which began at about 600°C and ended at around 900°C. It was correlated to the conversion from the anhydrous rhabdophane precursors into monazite-cheralite solid solutions. Indeed, the monazite-type structure is more compact than the rhabdophane counterpart. As a matter of example, and taking into account a similar number of unit formula per lattice for the two structures (Z = 3), the unit cell volume shifted from V = 273.34(1) $Å^3$ for $SmPO_4$ anhydrous rhabdophane to V = 211.7(1) – 214.15(1) $Å^3$ for monazite [13, 28, 38, 39], resulting in a volumic shrinkage of more than 20%. This value is then in good agreement with the linear shrinkage measured in this work. Despite this important volume drop, no significant crack formation was observed at this stage, but slight deformation of the cylindrical shape was noted in some cases (especially when sintering the pellets at 1200°C). Finally, the last shrinkage step evidenced on the dilatometric curve was observed typically above 1000°C and was correlated to the sintering of the

samples. This result fits well with our previous study [15] and with the data reported by Bregiroux *et al.* for the direct sintering of rhabdophane-type $LaPO_4$ [17].

Moreover, it is to note that, for all the samples, the densification took place between 1000°C and 1300°C since no additional shrinkage was observed above this temperature. This range of temperatures was then significantly lower than that reported by Glorieux *et al.* for the densification of $La_{0.73}Ce_{0.09}Th_{0.09}Ca_{0.09}PO_4$, synthesized by solid-state reaction (1200°C - 1600°C) [22]. Besides, the temperature of the highest densification rate (minimum of the derivative curve) was systematically found below 1200°C in this study while that of $La_{0.73}Ce_{0.09}Th_{0.09}Ca_{0.09}PO_4$ lied between 1300-1400°C. The direct sintering of Th-bearing rhabdophanes then led the densification temperature to decrease significantly, which is probably due to the high specific surface area and the good cationic homogeneity of the initial powders.

Additionally, even though Glorieux observed a two-step shrinkage during the sintering of the $La_{0.73}Ce_{0.09}Th_{0.09}Ca_{0.09}PO_4$ monazite-cheralite, the shrinkage obtained in this study during direct sintering from rhabdophane was more likely a one-step process according to the derivative curves, as reported by Bregiroux for $LnPO_4$ end-members [17, 22]. In this framework, Glorieux suggested that the first stage of shrinkage was due to densification while the second, caused by grain growth, would take place at a higher temperature, however with a close gap, *i.e.* 1320°C and 1390°C. In this study, however, the densification took place at a much lower temperature (below 1200°C) and proceeded much faster. Therefore, the grain growth process might have begun at a lower temperature leading to the disappearance of the second minimum peak on the derivative curve.

It is also worth noting that the temperature associated with the maximum densification rate globally increased with the Th-Ca doping. However, for the lowest substitution rate investigated, *i.e.* for x = 0.05, the densification took place at a lower temperature than for the $NdPO_4{\cdot}nH_2O$ end-member (about 1000°C for x = 0.05 and 1070°C for x = 0.00). According to the previous reports on the sintering of Sr-doped $LaPO_4{\cdot}nH_2O$ rhabdophane [40], the incorporation of a divalent ion in the structure could create oxygen vacancies which could accelerate the densification for $Nd_{0.09}Ca_{0.05}Th_{0.05}PO_4$. Nevertheless, the temperature related to the end of the densification process was almost the same for these two samples, i.e. about 1150°C, while that of x = 0.075 was about 1300°C and 1400°C for x = 0.10.

In our study, the incorporation of thorium typically above x = 0.05 seems to inhibit the densification and leads to higher sintering temperatures. This observation contradicts the results of Montel *et al.* who reported that the shrinkage of $La_{0.73}Ce_{0.08}Ca_{0.09}Th_{0.09}PO_4$ monazite-cheralite solid solution was more efficient than that of pure monazite end-member during a similar dilatometry test [21]. Considering that their $La_{0.73}Ce_{0.08}Ca_{0.09}Th_{0.09}PO_4$ precursor was synthesized through solid-state reaction, one could suggest that local heterogeneities might have accelerated the densification step. Conversely, the rhabdophane precursor obtained during our work by hydrothermal synthesis presents a

better homogeneity in terms of cation distribution. Consequently, solute drag effects might operate due to the segregation of thorium towards grain boundaries, leading the grain growth to slow down. Such mechanism is well known and was reported for several kinds of ceramic materials such as oxides [41], titanates [42] or niobiates [43].

The Dorn's method was also applied in order to determine the activation energy associated with the densification process (**Table 3**). In order to avoid any bias due to the rhabdophane-monazite conversion occurring at about 800°C, the temperature range of the isothermal heat treatments was set from 1000 to 1500°C. For $NdPO_4$ and $Nd_{0.9}Th_{0.05}Ca_{0.05}PO_4$ samples, the densification was fast and appeared to be complete at 1100°C, which led to consider only one or two temperature interval to assess E_A values. For x = 0.075 and x = 0.1, the densification ended at about 1250°C and five values were obtained for each composition, which allowed us to determine average activation energies. The activation energy determined for pure $NdPO_4$, *i.e.* E_A = 530 ± 90 kJ.mol^{-1} [44] appeared to be in excellent agreement with that reported by Bregiroux *et al.* for $LaPO_4$ (532 ± 80 kJ.mol-^{1}). For x = 0.05, the activation energy was significantly lower than for other compositions, which could explain its faster densification. Conversely, with higher Ca-Th coupled substitution, the activation energy increased. Even though, for x = 0.075 and x = 0.1, it remained slightly lower than that obtained for $NdPO_4$. However, as their specific surface area was about half of the monazite end-member, the densification was still found to be slower than for $NdPO_4$.

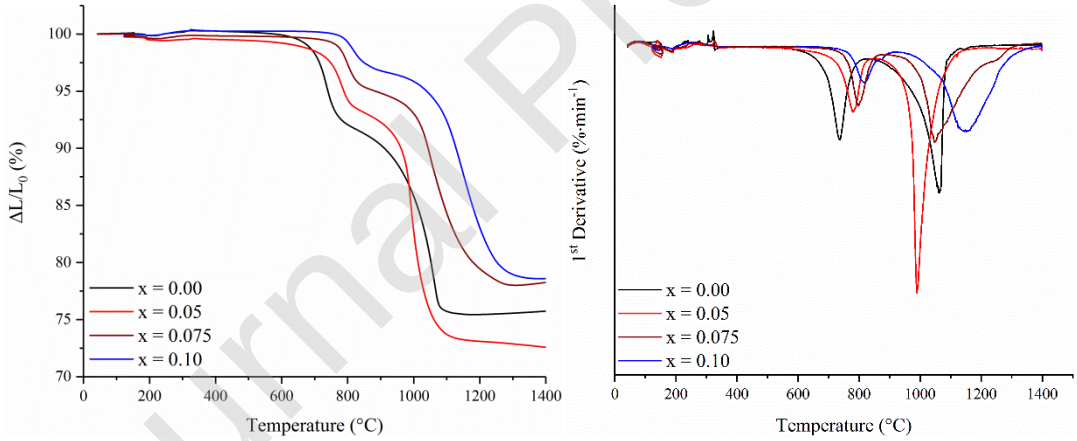

Figure 3. Dilatometry curves and associated derivative plots obtained from $Nd_{1-2x}Th_xCa_xPO_4 \cdot nH_2O$ pellets.

Table 3. The average activation energies determined for $Nd_{1-2x}Th_xCa_xPO_4$ solid solutions using Dorn's method.

x	0.00	0.05	0.075	0.10
E_A (kJ·mol^{-1})	530 ± 90	360 ± 90	440 ± 120	480 ± 130

3.3. Establishment of sintering map

The sintering map usually demonstrates the variation of the grains mass median diameter (D_{50}) versus the relative density under different sintering conditions, *e.g.* temperature, heating time, chemical composition, etc. It is thereby of great interest in the aim to control the final microstructure of ceramic materials, including radioactive waste forms. According to the dilatometry study above, the linear shrinkage of $Nd_{1-2x}Ca_xTh_xPO_4$ solid solution was systematically found to be complete above 1200°C. Three temperature set points, *i.e.* 1200°C, 1300°C, and 1400°C were then considered while the sintering time window varied from 1 to 8 h.

3.3.1. Density measurements

The evolution of the relative density measured by the geometrical method is presented in **Figure 4**. Despite the variation of the composition, the density of the pellets systematically reached 95 %TD after heating at least 4 hours at 1400°C, which evidenced that direct sintering from as-synthesized rhabdophane precursors could yield to highly densified monazite-cheralite type ceramics. Nevertheless, the Th-Ca coupled substitution clearly inhibited the densification. Indeed, the densification was complete after only 4 hours at 1200 °C for $NdPO_4$ while high-density $Nd_{0.8}Ca_{0.1}Th_{0.1}PO_4$ pellets were only obtained at 1400 °C. Accordingly, He-pycnometry measurements (see **Table 4**) showed that higher temperatures and longer sintering times were required to fully eliminate the open porosity and start removing the closed one when Th/Ca co-substitution rate increased.

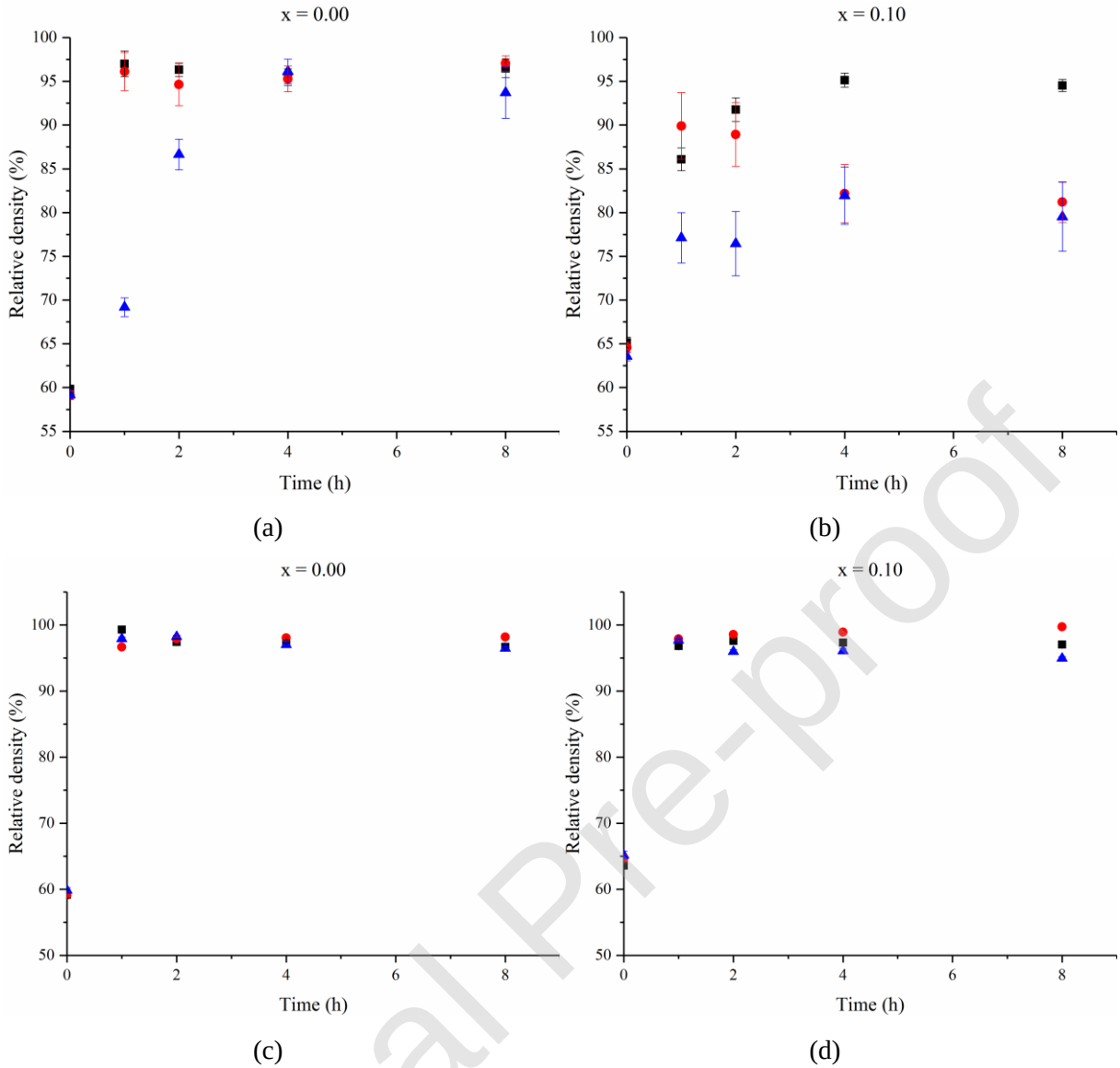

Figure 4. Evolution of relative density vs time at different temperatures (▲ 1200 °C, ● 1300 °C and ■ 1400 °C) obtained for monazite-cheralite $Nd_{1-2x}Ca_xTh_xPO_4$. The relative density was determined either by geometric measurement (a,b) or by helium pycnometry (c,d).

Table 4. Densities and D_{50} values obtained for the monazite-cheralite $Nd_{1-2x}Ca_xTh_xPO_4$ ceramic pellets.

x	Temperature (°C)	Time (h)	Bulk density (%)	Helium density (%)	Open porosity (%)	Closed porosity (%)	D_{50} (μm)
0.000	1200	1	69 ± 1	99.3 ± 0.5	30 ± 1	0.7 ± 0.5	0.11 ± 0.07
0.000	1200	2	87 ± 2	97.4 ± 0.5	11 ± 2	2.6 ± 0.5	0.18 ± 0.08
0.000	1200	4	96 ± 1	97.6 ± 0.2	1 ± 1	2.4 ± 0.2	0.11 ± 0.07
0.000	1200	8	94 ± 3	96.7 ± 0.2	3 ± 3	3.3 ± 0.2	0.12 ± 0.10
0.000	1300	1	96 ± 2	96.7 ± 0.2	1 ± 2	3.3 ± 0.2	0.14 ± 0.13
0.000	1300	2	95 ± 2	97.9 ± 0.2	3 ± 2	2.1 ± 0.2	0.17 ± 0.19
0.000	1300	4	95 ± 1	98.1 ± 0.3	3 ± 1	1.9 ± 0.3	7.22 ± 6.94
0.000	1300	8	97 ± 1	98.2 ± 0.2	1 ± 1	1.8 ± 0.2	8.51 ± 7.68
0.000	1400	1	97 ± 1	97.9 ± 0.3	1 ± 1	2.1 ± 0.3	8.01 ± 6.80
0.000	1400	2	96 ± 1	98.2 ± 0.2	2 ± 1	1.8 ± 0.2	9.72 ± 8.32
0.000	1400	4	95 ± 1	97.0 ± 0.4	2 ± 1	3.0 ± 0.4	11.37 ± 9.68
0.000	1400	8	96 ± 1	96.5 ± 0.3	0 ± 1	3.5 ± 0.3	8.12 ± 7.21
0.050	1200	1	68 ± 2	100.3 ± 0.3	32 ± 2	0.0 ± 0.3	0.10 ± 0.05
0.050	1200	2	73 ± 4	99.7 ± 0.3	27 ± 4	0.3 ± 0.3	0.09 ± 0.06
0.050	1200	4	85 ± 3	97.5 ± 0.2	13 ± 3	2.5 ± 0.2	0.12 ± 0.09
0.050	1200	8	75 ± 5	99.2 ± 0.2	24 ± 5	0.8 ± 0.2	0.09 ± 0.08
0.050	1300	1	80 ± 4	97.3 ± 0.2	17 ± 4	2.7 ± 0.2	0.11 ± 0.13
0.050	1300	2	88 ± 4	98.8 ± 0.2	11 ± 4	1.2 ± 0.2	0.26 ± 0.27
0.050	1300	4	84 ± 4	97.6 ± 0.3	13 ± 4	2.4 ± 0.3	0.72 ± 0.78
0.050	1300	8	94 ± 1	96.5 ± 0.2	2 ± 1	3.5 ± 0.2	0.54 ± 0.25
0.050	1400	1	92 ± 2	96.8 ± 0.3	4 ± 2	3.2 ± 0.3	0.61 ± 0.31
0.050	1400	2	93 ± 1	96.9 ± 0.2	4 ± 1	3.1 ± 0.2	0.78 ± 0.42
0.050	1400	4	92 ± 2	95.9 ± 0.3	4 ± 2	4.1 ± 0.3	0.80 ± 0.67
0.050	1400	8	92 ± 3	96.2 ± 0.3	4 ± 3	3.8 ± 0.3	2.85 ± 2.24
0.075	1200	1	68 ± 2	100.1 ± 0.4	32 ± 2	0.0 ± 0.4	0.10 ± 0.07
0.075	1200	2	69 ± 3	99.5 ± 0.2	31 ± 3	0.5 ± 0.2	0.10 ± 0.08
0.075	1200	4	76 ± 4	97.5 ± 0.2	21 ± 4	2.5 ± 0.2	0.10 ± 0.08
0.075	1200	8	73 ± 4	98.4 ± 0.2	26 ± 4	1.6 ± 0.2	0.09 ± 0.06
0.075	1300	1	77 ± 3	94.3 ± 0.2	17 ± 3	5.7 ± 0.2	0.11 ± 0.10
0.075	1300	2	81 ± 6	100.2 ± 0.5	19 ± 6	0.0 ± 0.2	0.11 ± 0.14
0.075	1300	4	88 ± 3	98.8 ± 0.2	11 ± 3	1.2 ± 0.2	0.32 ± 0.21
0.075	1300	8	95 ± 2	98.0 ± 0.2	3 ± 2	2.0 ± 0.2	0.28 ± 0.26
0.075	1400	1	88 ± 2	98.7 ± 0.3	11 ± 2	1.3 ± 0.3	0.18 ± 0.11
0.075	1400	2	91 ± 1	98.2 ± 0.3	7 ± 1	1.8 ± 0.3	0.18 ± 0.15
0.075	1400	4	94 ± 1	97.3 ± 0.4	3 ± 1	2.7 ± 0.4	0.97 ± 0.58
0.075	1400	8	94 ± 1	96.7 ± 0.3	3 ± 1	3.3 ± 0.3	1.04 ± 0.65
0.100	1200	1	77 ± 3	96.8 ± 0.3	20 ± 3	3.2 ± 0.3	0.09 ± 0.06
0.100	1200	2	76 ± 4	97.6 ± 0.2	21 ± 4	2.4 ± 0.2	0.09 ± 0.07
0.100	1200	4	82 ± 3	97.3 ± 0.2	16 ± 3	2.7 ± 0.2	0.08 ± 0.06
0.100	1200	8	79 ± 4	97.0 ± 0.2	18 ± 4	3.0 ± 0.2	0.11 ± 0.11
0.100	1300	1	90 ± 4	97.9 ± 0.2	8 ± 4	2.1 ± 0.2	0.09 ± 0.09

x	Temperature (°C)	Time (h)	Bulk density (%)	Helium density (%)	Open porosity (%)	Closed porosity (%)	D_{50} (µm)
0.100	1300	2	89 ± 4	98.6 ± 0.2	10 ± 4	1.4 ± 0.2	0.08 ± 0.11
0.100	1300	4	82 ± 3	98.9 ± 0.2	17 ± 3	1.1 ± 0.2	0.11 ± 0.11
0.100	1300	8	81 ± 2	99.7 ± 0.3	19 ± 2	0.3 ± 0.3	0.11 ± 0.11
0.100	1400	1	86 ± 1	97.7 ± 0.3	12 ± 1	2.3 ± 0.3	0.28 ± 0.14
0.100	1400	2	92 ± 1	96.0 ± 0.3	4 ± 1	4.0 ± 0.3	0.41 ± 0.20
0.100	1400	4	95 ± 1	96.1 ± 0.4	1 ± 1	3.9 ± 0.4	1.14 ± 0.53
0.100	1400	8	94 ± 1	94.9 ± 0.3	1 ± 1	5.1 ± 0.3	1.32 ± 0.74

3.3.2. SEM observation and Grain size determination

The SEM images presented in **Figure 5** confirmed that highly dense samples were obtained for all the Ca/Th doping rates studied after heating at 1400 °C for 8h. Also, the grains exhibited oblong-polygon morphology which was in good agreement with the work of Arinicheva *et al.* who reported that the use of precursors with initial needle-like morphology could result in dense ceramic with elongated grains [20]. For $NdPO_4$ end-member, the maximum length of the grains was about 50 µm with a width around 15 µm. On the other hand, the Th-Ca co-substitution was found to inhibit the grain growth, with D_{50} decreasing from 8.1 µm to 1.3 µm while the co-substitution rate increased from x = 0 to x = 0.1.

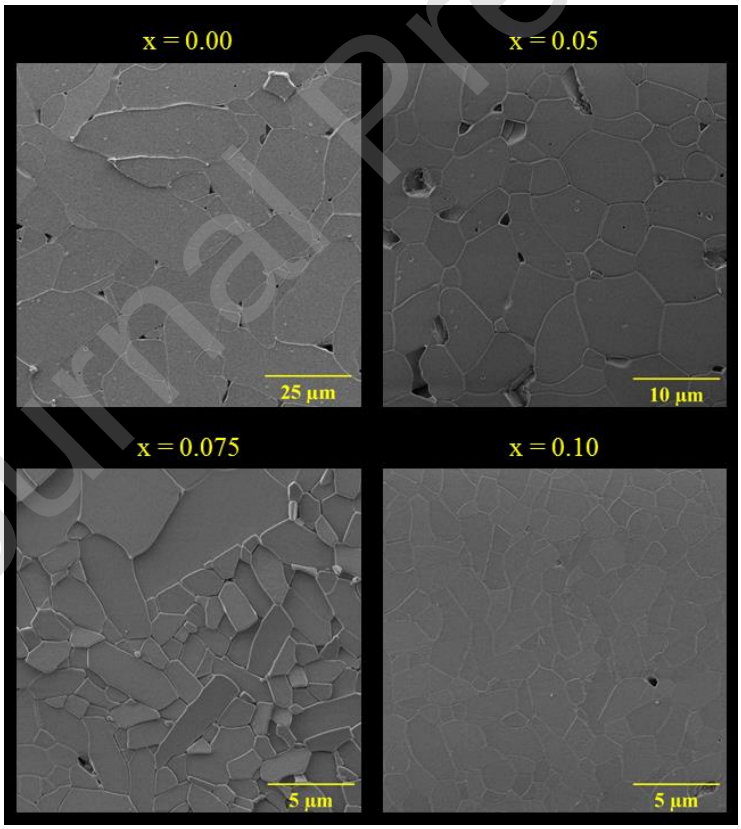

Figure 5. SEM micrographs obtained for $Nd_{1-2x}Ca_xTh_xPO_4$ pellets after sintering at 1400 °C during 8h.

Apart from the chemical composition, the temperature appeared as a very important factor driving the average grain size. For $Nd_{0.80}Ca_{0.1}Th_{0.1}PO_4$, D_{50} reached 0.11 µm after heating at 1200°C for 8h, meaning that no significant grain growth occurred at this temperature (**Figure 6**). Additionally, several pores were observed, which was consistent with the relative density value determined (79 ± 4 %TD). At 1300°C, the grain size increased slightly as the D_{50} was 0.24 µm. However, the pore contribution was not reduced and the relative density remained similar (81 ± 2 %TD). Conversely, the grain size increased by about one order of magnitude after heating at 1400°C (1.32 µm) while open pores were significantly eliminated, leading to a dense ceramic with 94 ± 1 %TD. Consequently, in order to obtain high-density $Nd_{0.80}Ca_{0.1}Th_{0.1}PO_4$ ceramics, the sintering temperature should be equal to 1400°C. For other compositions, however, the sintering temperature could be lower. As instance, $NdPO_4$ could reach 97 ± 1 %TD with D_{50} = 8.5 µm after only 8 hours at 1300°C.

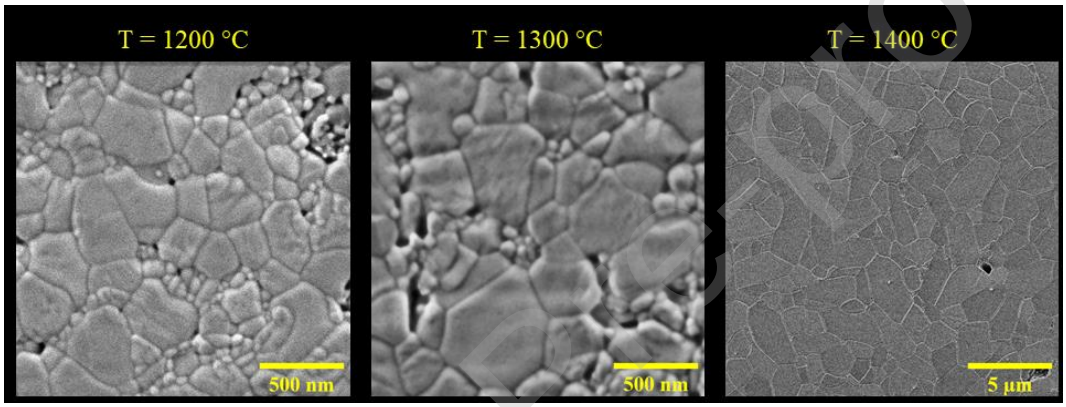

Figure 6. SEM micrographs obtained for $Nd_{0.80}Ca_{0.1}Th_{0.1}PO_4$ pellets after sintering during 8h at different temperatures.

Finally, the impact of the sintering time was also investigated (**Figure 7**). At 1400 °C, the grain size of $Nd_{0.80}Ca_{0.1}Th_{0.1}PO_4$ grew significantly over time, i.e. from 0.28 µm after 1h to 1.32 µm after 8h. At the same time, the open porosity dropped down, leading the relative density to increase from 86 ± 1 to 94 ± 1 %TD. It is also worth noting that the pellet sintered at 1400°C for 1h exhibited slightly bigger grain size and higher density than that prepared at 1300°C for 8h, which indicated that temperature had a stronger impact on the sintering process compared to heat duration.

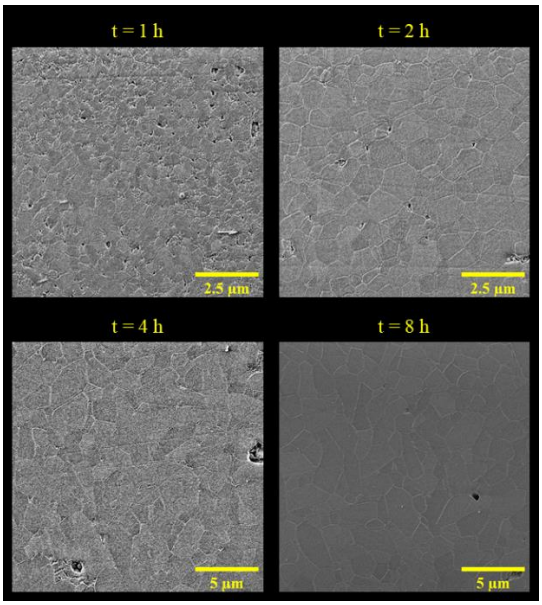

Figure 7. SEM micrographs obtained for $Nd_{0.80}Ca_{0.1}Th_{0.1}PO_4$ pellets after sintering at 1400°C during different sintering times.

Also, it is important to underline that for all the samples studied, the grain size distribution followed a log-normal distribution (**Figures 8 and S2**), in agreement with previous reports [21, 22, 45]. Moreover, self-similarity, which accounted for the invariance of the normalized grain size distribution versus time, was checked under any sintering condition despite the change of temperature or chemical composition [20, 24, 46]. Hence, no abnormal grain growth phenomena occurred during the sintering of $Nd_{1-2x}Ca_xTh_xPO_4$ monazite-cheralite solid solutions.

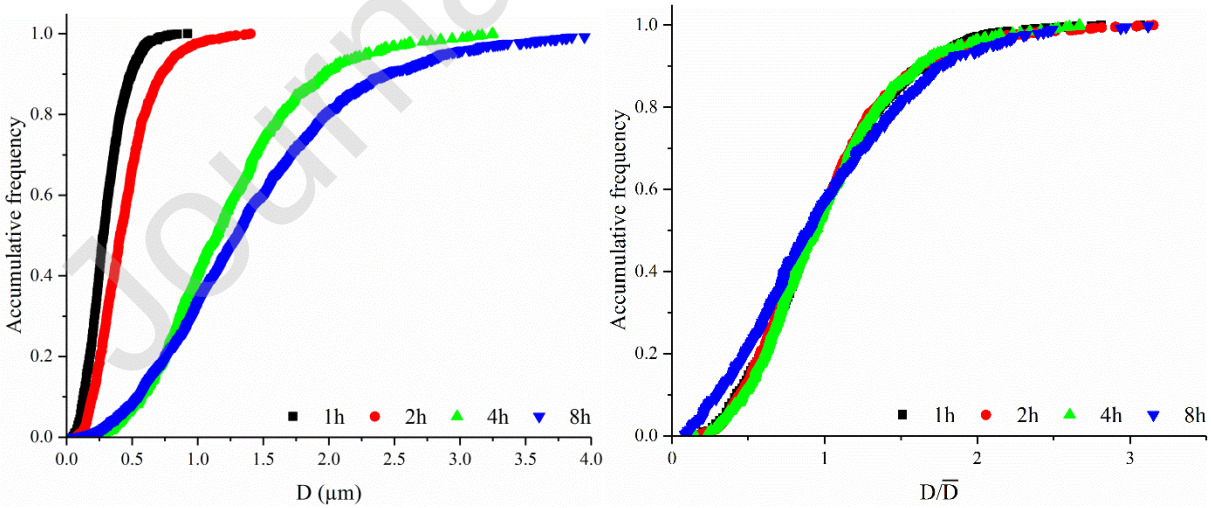

Figure 8. Cumulative Grain size distribution obtained for $Nd_{0.80}Ca_{0.1}Th_{0.1}PO_4$ vs sintering time at 1400°C.

3.3.3. *Sintering map*

After the determination of bulk relative densities and grain sizes (D_{50}), the sintering trajectories of $Nd_{1-2x}Ca_xTh_xPO_4$ solid solutions were finally built up (**Figure 9**). All the 48 tests were first gathered according to the sintering temperature. At 1200°C, the grain growth appeared to be limited as D_{50} only increased from 0.08 to 0.24 µm. Conversely, the sintering was dominated by densification with relative density raising from 68 %TD to 96 %TD. This result then paves the way to the elaboration of highly dense ceramics with submicrometric microstructure. At 1400°C, most of the samples presented a relative density higher than 90 %TD while D_{50} range across 2 orders of magnitude (from 0.18 to 11.4 µm, depending on the chemical composition considered), which indicated that the densification was complete and the grain growth became the predominant behavior. On this basis, samples sintered at 1300°C exhibited an intermediate behavior, where both densification and grain growth played important roles, leading pellet density to raise from 77 %TD to 97 %TD and D_{50} to increase from 0.08 to 8.5 µm.

Finally, all the samples were grouped according to their chemical composition (**Figure 9b**). As already discussed previously, the Ca/Th coupled substitution seemed to inhibit both densification and grain growth. For $NdPO_4$ end-member, all the prepared samples usually presented a high relative density (> 90 %TD) and could reach an important grain size (D_{50} > 8 µm) when heating at 1300-1400°C. Therefore, they were mostly located on the top right region of the sintering map. With the increase of the substitution rate, the samples gradually occupied the lower left region. As a matter of example, the maximum D_{50} value for $Nd_{0.80}Ca_{0.1}Th_{0.1}PO_4$ samples was 1.3 µm which was an order of magnitude smaller than the $NdPO_4$ end-member (11.4 µm).

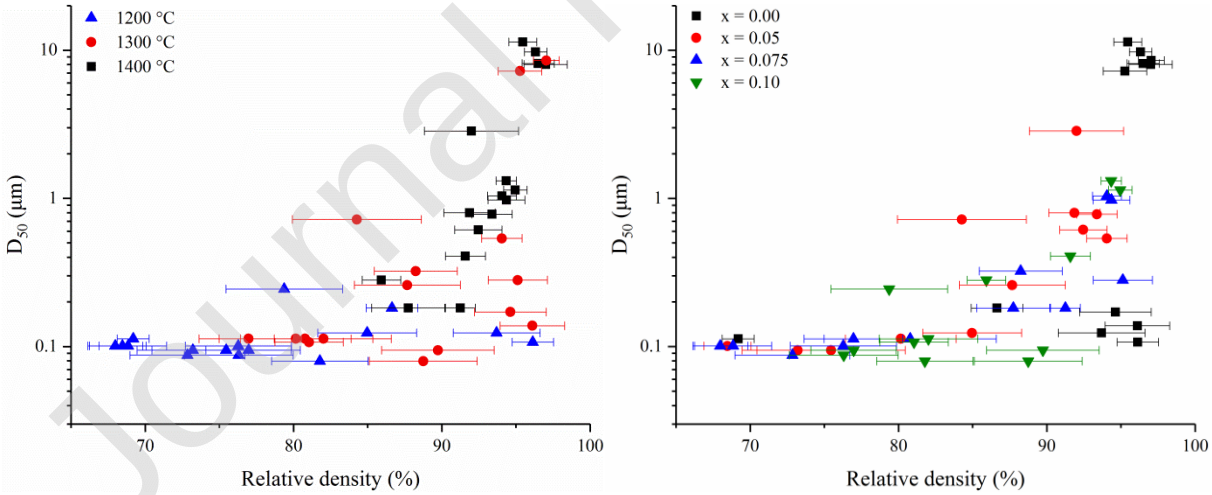

(a) (b)

Figure 9. Sintering map obtained for $Nd_{1-2x}Ca_xTh_xPO_4$ ceramics. All the samples are gathered depending on their sintering temperature (a) or on their chemical composition (b).

3.4. Microhardness

The microhardness of the $Nd_{1-2x}Ca_xTh_xPO_4$ ceramics was determined by using the Vickers hardness test. All the pellets were sintered at 1400°C for 8h in order to produce dense ceramics and then polished to reach a mirror-grade surface. According to the previous reports, the microhardness determined by Vickers test depended on the loading force [18, 44]. If the loading force was too high, the material around the indenter broke, leading to underestimate the microhardness. As a result, the $NdPO_4$ pellet was firstly indented with different loads from 0.1 to 2 N in order to optimize the loading force. In this test, ten measurements were performed randomly on the polished surface for each loading force so that the average microhardness was determined. The collected results presented no significant variation when the loading force increased from 0.1 N to 0.5 N (**Figure 10**). However, for $F \geq 1$ N, the microhardness decreased significantly. Hence, the applied loading force was chosen to 0.25 N in the following tests.

During the hardness determination, each pellet underwent 15 measurements randomly located on its polished surface to obtain the average hardness. For $NdPO_4$, the microhardness determined in this work reached 4.9 ± 0.8 GPa, which was in agreement with the value reported by Bregiroux *et al.* [44]. The influence of the Ca-Th coupled substitution was further found to be negligible (**Table 5**). Indeed, even if a slightly lower value was measured for x = 0.05 compared to other samples, the associated large uncertainty led to conclude that the microhardness of $Nd_{1-2x}Ca_xTh_xPO_4$ ceramics pellets remained unchanged. It is then in the same order of magnitude that the Vicker's hardness determined for several other phosphate-based ceramic wasteforms envisaged for the specific conditioning of actinides, such as fluorapatite (3.7 GPa) [47], β-TPD (4.4 GPa) [48] or NZPs (5.9 GPa) [49]. Also, it appears to be only slightly below the value reported by Popa *et al.* for the $CaTh(PO_4)_2$ cheralite end-member sintered by SPS technique [50].

Table 5. Microhardness obtained for $Nd_{1-2x}Ca_xTh_xPO_4$ ceramics.

X	0.00	0.05	0.075	0.10
Hv (GPa)	4.9 ± 0.8	4.5 ± 0.8	4.9 ± 0.7	5 ± 0.5

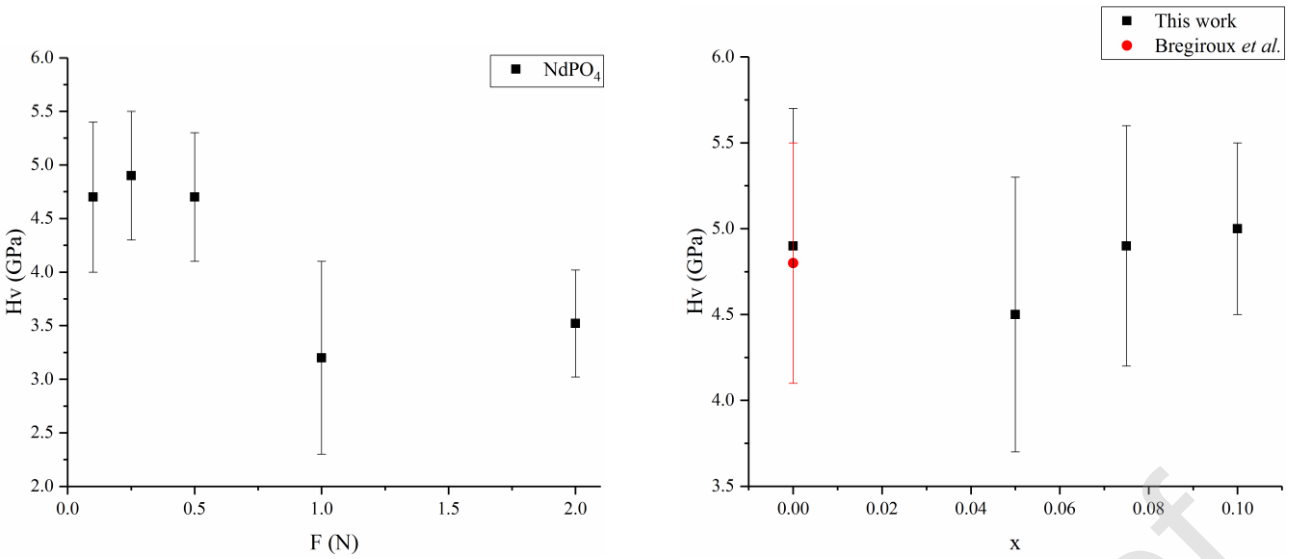

(a) (b)

Figure 10. Evolution of microhardness of $NdPO_4$ vs loading force (a) and of the microhardness (b) obtained for $Nd_{1-2x}Ca_xTh_xPO_4$ ceramics [44].

4. Conclusion

The results obtained during this study pave the way to an innovative process for the elaboration of highly densified and homogeneous $Nd_{1-2x}Ca_xTh_xPO_4$ ($x = 0 – 0.1$) monazite-cheralite wasteforms. Indeed, their direct sintering from rhabdophane-type precursors was found to result in homogeneous high-density pellets, and significantly lowered the sintering temperature compared to solid-state reactions previously reported in the literature. Such a dustless process thus avoided any additional step of heating or mechanical grinding that are often considered to be potentially contaminating.

The sintering map of the $Nd_{1-2x}Ca_xTh_xPO_4$ solid solution was further established. No significant grain growth was observed at 1200°C and the densification appeared to be the predominant behavior. Conversely, the complete densification quickly operated at 1400°C and was followed by considerable grain growth. However, the Th-Ca coupled substitution seemed to inhibit both densification and grain growth mechanisms, leading to the decrease of the maximum grain size (D_{50}) by an order of magnitude. Concomitantly, the activation energy associated with the densification was found between 361 ± 90 and 530 ± 90 $kJ.mol^{-1}$, depending on the chemical composition considered.

Finally, the microhardness of the $Nd_{1-2x}Ca_xTh_xPO_4$ ceramics determined by the Vickers hardness test was about 4.9 ± 0.8 GPa, which is in the typical range of the values determined for phosphate-based wasteforms designed for actinides conditioning. Beyond a deeper investigation of the mechanical properties (such as bending strength and fracture toughness), the next studies will now be devoted to the evaluation of the chemical durability of the sintered samples. In this frame, the sintering maps obtained

in this work will help in preparing dense pellets with significantly different grain sizes. These samples will further be used to evidence the impact of microstructure on the leaching behavior, particularly at the grain boundaries level where local composition variations can occur.

Declaration of interests

☒ The authors declare that they have no known competing financial interests or personal relationships that could have appeared to influence the work reported in this paper.

☐The authors declare the following financial interests/personal relationships which may be considered as potential competing interests:

Acknowledgment

Ph.D. of D.Q. was funded by the China Scholarship Council (CSC). The authors would like to thank R. Podor for his help in polishing the sintered samples.

Supplementary information:

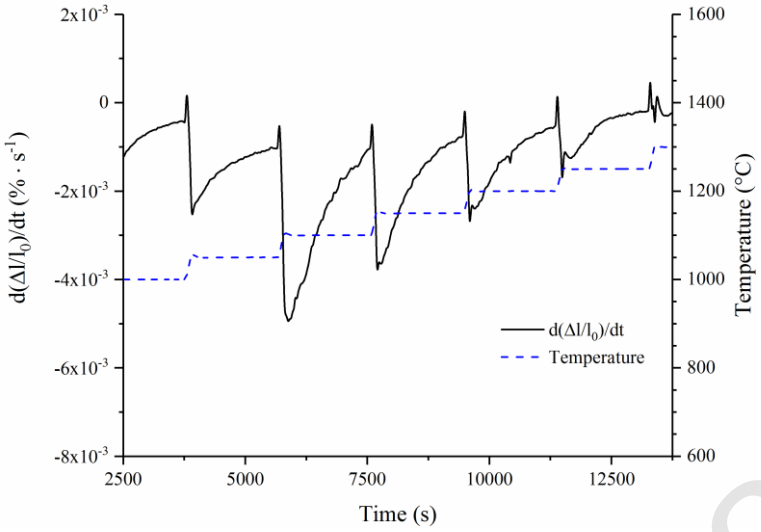

Figure S1. Determination of $Nd_{1-2x}Th_xCa_xPO_4$ sintering activation energy using the Dorn's method.

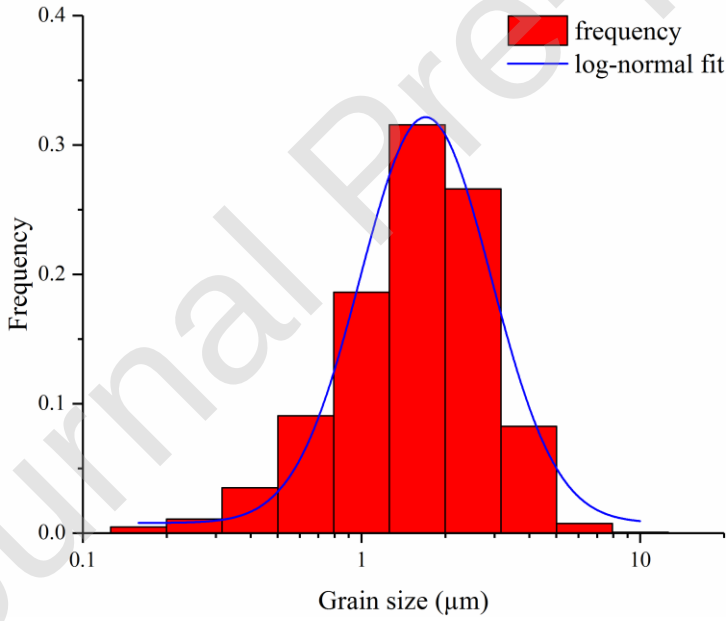

Figure S2. Grain size distribution obtained for $Nd_{0.80}Ca_{0.1}Th_{0.1}PO_4$ after heating at 1400°C for 8h.

References

[1] N. Dacheux, N. Clavier, R. Podor, Monazite as a promising long-term radioactive waste matrix: Benefits of high-structural flexibility and chemical durability, American Mineralogist 98(5-6) (2013) 833-847.

[2] L.A. Boatner, Synthesis, structure and properties of monazite, pretulite and xenotime, Rev. Miner. Geochem. 48 (2002) 87-120.

[3] B. Van Emden, M.R. Thornber, J. Graham, F.J. Lincoln, The incorporation of actinides in monazite and xenotime from placer deposits in Western Australia, Can. Miner. 35 (1997) 95-104.

[4] D. Bregiroux, O. Terra, F. Audubert, N. Dacheux, V. Serin, R. Podor, D. Bernache-Assollant, Solid-state synthesis of monazite-type compounds containing tetravalent elements, Inorg. Chem. 46(24) (2007) 10372-10382.

[5] D.D. Davis, E.R. Vance, G.J. McCarthy, Crystal chemistry and phase relations in the synthetic minerals of ceramic waste forms. II. Studies of uranium-containing monazites, Plenum Press, New York, United State, 1981.

[6] G.R. Lumpkin, T. Geisler-Wierwille, Minerals and Natural Analogues, Comprehensive Nuclear Materials, Elsevier, Oxford, 2012, pp. 563-600.

[7] L.A. Boatner, B.C. Sales, Monazite, in: W. Lutze, R.C. Ewing (Eds.), Radioactive Waste Forms for the Future, North-Holland Physics Publishing, Amsterdam, 1988, pp. 495-564.

[8] X. Deschanels, A.M. Seydoux-Guillaume, V. Magnin, A. Mesbah, M. Tribet, M.P. Moloney, Y. Serruys, S. Peuget, Swelling induced by alpha decay in monazite and zirconolite ceramics: A XRD and TEM comparative study, J Nucl Mater 448(1-3) (2014) 184-194.

[9] B.E. Burakov, M.A. Yagovkina, V.M. Garbuzov, A.A. Kitsay, V.A. Zirlin, Self-Irradiation of Monazite Ceramics: Contrasting Behavior of $PuPO_4$ and $(La,Pu)PO_4$ Doped with ^{238}Pu, MRS Proceedings 824 (2004).

[10] D. Bregiroux, R. Belin, P. Valenza, J., F. Audubert, D. Bernache-Assollant, Plutonium and americium monazite materials: Solid state synthesis and X-ray diffraction study, J Nucl Mater 366(1-2) (2007) 52-57.

[11] R. Podor, Synthèse et caractérisation des monazites uranifères et thorifères, Université Henri Poincaré Nancy I, 1994.

[12] Y. Hikichi, K. Hukuo, J. Shiokawa, Solid solutions in the system monazite ($CePO_4$) - Huttonite ($ThSiO_4$) and monazite - $(Ca_{0.5}Th_{0.5})PO_4$, 1978.

[13] Y.X. Ni, J.M. Hughes, A.N. Mariano, Crystal-Chemistry of the Monazite and Xenotime Structures, Am Mineral 80(1-2) (1995) 21-26.

[14] D. Qin, A. Mesbah, C. Gausse, S. Szenknect, N. Dacheux, N. Clavier, Incorporation of thorium in the rhabdophane structure: Synthesis and characterization of $Pr_{1-2x}Ca_xTh_xPO_4{\cdot}nH_2O$ solid solutions, J Nucl Mater 492 (2017) 88-96.

[15] D. Qin, A. Mesbah, N. Clavier, S. Szenknect, N. Dacheux, From Th-Rhabdophane to Monazite-Cheralite Solid Solutions: Thermal Behavior of $Nd_{1-2x}Th_xCa_xPO_4{\cdot}nH_2O$ (x = 0–0.15), Crystal Growth & Design 19(5) (2019) 2794-2801.

[16] Y. Hikichi, T. Ota, T. Hattori, Thermal, mechanical and chemical properties of sintered monazite-(La, Ce, Nd or Sm), Mineralogical Journal 19(3) (1997) 123-130.

[17] D. Bregiroux, S. Lucas, E. Champion, F. Audubert, D. Bernache-Assollant, Sintering and microstructure of rare earth phosphate ceramics $REPO_4$ with RE=La, Ce or Y, J Eur Ceram Soc 26(3) (2006) 279-287.

[18] Y. Arinicheva, A. Bukaemskiy, S. Neumeier, G. Modolo, D. Bosbach, Studies on thermal and mechanical properties of monazite-type ceramics for the conditioning of minor actinides, Prog Nucl Energ 72 (2014) 144-148.

[19] S. Neumeier, Y. Arinicheva, N. Clavier, R. Podor, A. Bukaemskiy, G. Modolo, N. Dacheux, D. Bosbach, The effect of the synthesis route of monazite precursors on the microstructure of sintered pellets, Progress in Nuclear Energy 92 (2016) 298-305.

[20] Y. Arinicheva, N. Clavier, S. Neumeier, R. Podor, A. Bukaemskiy, M. Klinkenberg, G. Roth, N. Dacheux, D. Bosbach, Effect of powder morphology on sintering kinetics, microstructure and mechanical properties of monazite ceramics, J Eur Ceram Soc 38(1) (2018) 227-234.

[21] J.-M. Montel, B. Glorieux, A.-M. Seydoux-Guillaume, R. Wirth, Synthesis and sintering of a monazite brabantite solid solution ceramic for nuclear waste storage, J Phys Chem Solids 67 (2006) 2489-2500.

[22] B. Glorieux, J.M. Montel, M. Matecki, Synthesis and sintering of a monazite–brabantite solid solution ceramics using metaphosphate, J Eur Ceram Soc 29(9) (2009) 1679-1686.

[23] N. Clavier, R. Podor, L. Deliere, J. Ravaux, N. Dacheux, Combining in situ HT-ESEM observations and dilatometry: An original and fast way to the sintering map of ThO_2, Materials Chemistry and Physics 137(3) (2013) 742-749.

[24] Y. Cherkaski, N. Clavier, L. Brissonneau, R. Podor, N. Dacheux, Densification behavior and microstructure evolution of yttrium-doped ThO_2 ceramics, Journal of the European Ceramic Society 37(10) (2017) 3381-3391.

[25] L. Perrière, D. Bregiroux, B. Naitali, F. Audubert, E. Champion, D.S. Smith, D. Bernache-Assollant, Microstructural dependence of the thermal and mechanical properties of monazite $LnPO_4$ (Ln=La to Gd), J Eur Ceram Soc 27(10) (2007) 3207-3213.

[26] C. Frontera, J. Rodriguez-Carvajal, FULLPROF as a new tool for flipping ratio analysis, Physica B-Condensed Matter 335(1-4) (2003) 219-222.

[27] P.E. Raison, S. Heathman, G. Wallez, C.E. Zvoriste, D. Bykov, G. Ménard, E. Suard, K. Popa, N. Dacheux, R.J.M. Konings, R. Caciuffo, Structure and nuclear density distribution in the cheralite—$CaTh(PO_4)_2$: studies of its behaviour under high pressure (36 GPa), Phys Chem Miner 39(8) (2012) 685-692.

[28] N. Clavier, R. Podor, N. Dacheux, Crystal chemistry of the monazite structure, Journal of the European Ceramic Society 31(6) (2011) 941-976.

[29] J. Schindelin, I. Arganda-Carreras, E. Frise, V. Kaynig, M. Longair, T. Pietzsch, S. Preibisch, C. Rueden, S. Saalfeld, B. Schmid, J.-Y. Tinevez, D.J. White, V. Hartenstein, K. Eliceiri, P. Tomancak, A. Cardona, Fiji: an open-source platform for biological-image analysis, Nature Methods 9 (2012) 676.

[30] A. Mesbah, N. Clavier, E. Elkaim, C. Gausse, I. Ben Kacem, S. Szenknect, N. Dacheux, Monoclinic Form of the Rhabdophane Compounds: $REEPO_4{\cdot}0.667H_2O$, Cryst Growth Des 14(10) (2014) 5090-5098.

[31] N. Dacheux, N. Clavier, A.-C. Robisson, O. Terra, F. Audubert, J.-É. Lartigue, C. Guy, Immobilisation of actinides in phosphate matrices, Cr Chim 7(12) (2004) 1141-1152.

[32] G. Wallez, P.E. Raison, N. Dacheux, N. Clavier, D. Bykov, L. Delevoye, K. Popa, D. Bregiroux, A.N. Fitch, R.J.M. Konings, Triclinic-Cubic Phase Transition and Negative Expansion in the Actinide IV (Th, U, Np, Pu) Diphosphates, Inorg Chem 51(7) (2012) 4314-4322.

[33] P. Benard, V. Brandel, N. Dacheux, S. Jaulmes, S. Launay, C. Lindecker, M. Genet, D. Louer, M. Quarton, $Th_4(PO_4)_4P_2O_7$, a new thorium phosphate: Synthesis, characterization, and structure determination, Chem Mater 8(1) (1996) 181-188.

[34] N. Dacheux, N. Clavier, G. Wallez, V. Brandel, J. Emery, M. Quarton, M. Genet, Characterization of the thorium phosphate-hydrogenphosphate hydrate (TPHPH) and study of its transformation into the thorium phosphate-diphosphate (β-TPD), Mater Res Bull 40(12) (2005) 2225-2242.

[35] H.Y.P. Hong, Crystal-Structures of Neodymium Metaphosphate (NdP_3O_9) and Ultraphosphate (NdP_5O_{14}), Acta Crystallogr B 30 (1974) 468-474.

[36] R.C.L. Mooney, Crystal structures of a series of rare earth phosphates, J Chem Phys 16(10) (1948) 1003-1003.

[37] A. Mesbah, N. Clavier, E. Elkaim, S. Szenknect, N. Dacheux, In pursuit of the rhabdophane crystal structure: from the hydrated monoclinic $LnPO_4.0.667H_2O$ to the hexagonal $LnPO_4$ (Ln = Nd, Sm, Gd, Eu and Dy), Journal of Solid State Chemistry 249 (2017) 221-227.

[38] D.F. Mullica, D.A. Grossie, L.A. Boatner, Structural refinements of praseodymium and neodymium orthophosphate, J Solid State Chem 58(1) (1985) 71-77.

[39] S.V. Ushakov, K.B. Helean, A. Navrotsky, L.A. Boatner, Thermochemistry of rare-earth orthophosphates, J Mater Res 16(9) (2011) 2623-2633.

[40] M.T. Colomer, Effect of Sr^{2+} doping on sintering behavior, microstructural development and electrical properties of $LaPO_4 \cdot nH_2O$ nanorods prepared by dry mechanical milling, Int J Hydrogen Energ 43(29) (2018) 13462-13474.

[41] P.L. Chen, I.W. Chen, Grain growth in CeO_2: Dopant effects, defect mechanism, and solute drag, J Am Ceram Soc 79(7) (1996) 1793-1800.

[42] A.C. Caballero, J.F. Fernandez, C. Moure, P. Duran, Effect of residual phosphorus left by phosphate ester on $BaTiO_3$ ceramics, Mater Res Bull 32(2) (1997) 221-229.

[43] H. Naceur, A. Megriche, M. El Maaoui, Effect of sintering temperature on microstructure and electrical properties of $Sr_{1-x}(Na_{0.5}Bi_{0.5})_xBi_2Nb_2O_9$ solid solutions, J Adv Ceram 3(1) (2014) 17-30.

[44] D. Bregiroux, Synthèse par voie solide et frittage de céramiques à structure monazite : application au conditionnement des actinides mineurs, 2005, pp. 1 vol. (VI-215 p.).

[45] D. Bregiroux, F. Audubert, D. Bernache-Assollant, Densification and grain growth during solid state sintering of $LaPO_4$, Ceram Int 35(3) (2009) 1115-1120.

[46] A. Maitre, D. Beyssen, R. Podor, Modelling of the grain growth and the densification of SnO_2-based ceramics, Ceram Int 34(1) (2008) 27-35.

[47] X.N. Gao, Y. Huang, Y.C. Teng, M.H. Yan, H.B. Zhang, X.G. Tuo, S.M. Peng, Fabrication and chemical durability of hot-pressed Na-bearing fluorapatite-type $Ca_8Sm_1Na_1(PO_4)_6F_2$ ceramic for immobilization of trivalent minor actinide, J Nucl Mater 507 (2018) 297-305.

[48] N. Dacheux, B. Chassigneux, V. Brandel, P. Le Coustumer, M. Genet, G. Cizeron, Reactive sintering of the thorium phosphate-diphosphate. Study of physical, thermal, and thermomechanical properties and chemical durability during leaching tests, Chem Mater 14(7) (2002) 2953-2961.

[49] A.I. Orlova, V.Y. Volgutov, D.A. Mikhailov, D.M. Bykov, V.A. Skuratov, V.N. Chuvil'deev, A.V. Nokhrin, M.S. Boldin, N.V. Sakharov, Phosphate $Ca_{1/4}Sr_{1/4}Zr_2(PO_4)_3$ of the $NaZr_2(PO_4)_3$ structure type: Synthesis of a dense ceramic material and its radiation testing, J Nucl Mater 446(1-3) (2014) 232-239.

[50] K. Popa, M. Cologna, L. Martel, D. Staicu, A. Cambriani, M. Ernstberger, P.E. Raison, J. Somers, $CaTh(PO_4)_2$ cheralite as a candidate ceramic nuclear waste form: Spark plasma sintering and physicochemical characterisation, J Eur Ceram Soc 36(16) (2016) 4115-4121.